

Towards a robust criterion of anomalous diffusion

Vittoria Sposini ¹, Diego Krapf ^{2,3}, Enzo Marinari^{4,5}, Raimon Sunyer ⁶, Felix Ritort ⁷,
Fereydoon Taheri ⁸, Christine Selhuber-Unkel⁸, Rebecca Benelli⁹, Matthias Weiss⁹, Ralf Metzler ^{10,11}✉ &
Gleb Oshanin¹²

Anomalous-diffusion, the departure of the spreading dynamics of diffusing particles from the traditional law of Brownian-motion, is a signature feature of a large number of complex soft-matter and biological systems. Anomalous-diffusion emerges due to a variety of physical mechanisms, e.g., trapping interactions or the viscoelasticity of the environment. However, sometimes systems dynamics are erroneously claimed to be anomalous, despite the fact that the true motion is Brownian—or vice versa. This ambiguity in establishing whether the dynamics as normal or anomalous can have far-reaching consequences, e.g., in predictions for reaction- or relaxation-laws. Demonstrating that a system exhibits normal- or anomalous-diffusion is highly desirable for a vast host of applications. Here, we present a criterion for anomalous-diffusion based on the method of power-spectral analysis of single trajectories. The robustness of this criterion is studied for trajectories of fractional-Brownian-motion, a ubiquitous stochastic process for the description of anomalous-diffusion, in the presence of two types of measurement errors. In particular, we find that our criterion is very robust for subdiffusion. Various tests on surrogate data in absence or presence of additional positional noise demonstrate the efficacy of this method in practical contexts. Finally, we provide a proof-of-concept based on diverse experiments exhibiting both normal and anomalous-diffusion.

¹Faculty of Physics, University of Vienna, Kolingasse 14-16, A-1090 Vienna, Austria. ²Department of Electrical and Computer Engineering, Colorado State University, Fort Collins, CO 80523, USA. ³School of Biomedical Engineering, Colorado State University, Fort Collins, CO 80523, USA. ⁴Dipartimento di Fisica, Sapienza Università di Roma, P.le A. Moro 2, I-00185 Roma, Italy. ⁵INFN, Sezione di Roma 1 and Nanotech-CNR, UOS di Roma, P.le A. Moro 2, I-00185 Roma, Italy. ⁶Departament de Biomedicina, Facultat de Medicina, Unitat de Biofísica i Bioenginyeria, Universitat de Barcelona, Diagonal 647, 08028 Barcelona, Spain. ⁷Small Biosystems Lab, Condensed Matter Physics Department, Facultat de Física, Universitat de Barcelona, Diagonal 647, 08028 Barcelona, Spain. ⁸Institute for Molecular Systems Engineering and Advanced Materials (IMSEAM), Heidelberg University, INF 225, 69120 Heidelberg, Germany. ⁹Experimental Physics I, University of Bayreuth, D-95440 Bayreuth, Germany. ¹⁰Institute of Physics and Astronomy, University of Potsdam, Karl-Liebknecht-Str 24/25, 14476 Potsdam-Golm, Germany. ¹¹Asia Pacific Centre for Theoretical Physics, Pohang 37673, Republic of Korea. ¹²Sorbonne Université, CNRS, Laboratoire de Physique Théorique de la Matière Condensée (UMR 7600), 4 Place Jussieu, 75252 Paris, Cedex 05, France. ✉email: rmetzler@uni-potsdam.de

The exploration of the dynamic properties of complex systems has been massively boosted by modern microscopic techniques allowing single-particle tracking (SPT) of micron- and submicron-sized tracers or even single molecules. SPT is routinely used to probe the local properties of materials and even live biological cells and tissue by passive and active microrheology¹. SPT now is a key tool to interrogate the structure–function relationships in biophysical applications^{2,3}, and it plays a central role in uncovering thermal and energy-fuelled intracellular transport of tracer particles or single molecules in biological cells and tissues⁴. SPT is thus at the heart of the newly emerging era of quantitative life sciences^{2–31}. Specifically, SPT unveiled different intracellular motion patterns of virus particles¹⁰, Cajal bodies¹², molecular motor-driven transport^{15,17,23}, the motion of telomeres^{25,32}, green fluorescent proteins²¹, DNA-binding proteins^{18,19}, mRNA molecules^{5,22,26}, membrane proteins^{11,13,20}, or endogenous granules^{24,27} and vesicles²⁸. SPT has also revealed protein interactions¹⁶ as well as key details of submicron tracer motion in mammalian cells¹⁴ and in the movement ecology of larger animals^{30,33}.

In contrast to pre-averaged data such as those obtained from fluorescence correlation spectroscopy (FCS) or fluorescence recovery after photobleaching (FRAP), SPT provides high-resolution “unprocessed” data: As raw data of test particle trajectories, SPT offers the best possible basis for statistical analysis³⁴. Indeed, a large toolbox of methods is available for analysing position time series X_t . Frequently, these data have revealed that particles exhibit an anomalous diffusion behaviour, defined by the power-law dependence $\langle X_t^2 \rangle \simeq t^\alpha$ of the mean squared displacement (MSD), where the angular brackets denote averaging over different realisations of recorded trajectories. The anomalous diffusion exponent α is commonly used to tell whether normal (Brownian, $\alpha = 1$) or anomalous diffusion ($\alpha \neq 1$) is observed. Here, the regimes of sub- and superdiffusion correspond to $0 < \alpha < 1$ and $\alpha > 1$, respectively. Distinguishing normal from anomalous diffusion is vital for predicting various characteristics of the systems under investigation—e.g., the diffusion-control of molecular reactions or the relaxation dynamics after manipulating the system—eventually allowing us to understand the actual physical mechanisms underlying the observations.

Fitting the scaling exponent α to finite measured time series is known to be a major challenge. For instance, contamination of the true trajectories by measurement noise was shown to lead to the erroneous conclusion to observe anomalous diffusion ($\alpha \neq 1$)³⁵. There exist methods to alleviate this problem, e.g., the mean-maximal excursion statistics³⁶. Moreover, Bayesian-maximum-likelihood methods^{37–39}, deep learning strategies^{40–45}, or feature-based methods^{42,43,46,47} also provide the best estimates for α . However, all these methods have their shortcomings. Quite severely, α values (along with D values^{48,49}) retrieved from fitting the MSD $\langle X_t^2 \rangle$ will vary from one trajectory to the next due to finite statistics within single trajectories. Indeed, trajectories from real experiments display different regimes with different scaling exponents^{37,38,50}, or due to the spatial heterogeneity of the environment^{51,52}. This leads to strong variability in the scaling exponents measured for different trajectories and renders predictions based on such fitting procedures even less accurate. Moreover, for realistic situations with α values closer to the Brownian value $\alpha = 1$, it becomes increasingly difficult to distinguish anomalous from Brownian motion⁴³. This latter caveat is further exacerbated when considering the unavoidable experimental sources of error in many SPT setups, especially when based on fluorescence microscopy methods.

Likely the most notorious source of uncertainty is the static localisation error that arises from the finite number of fluorescence photons garnered during an image of the particle from

which its position will be retrieved by elaborate tracking schemes: Each of these photons is emitted from a point-like source in the sample (the emitting fluorophore) and will hence be captured on a locus of the camera sensor according to the microscope’s point-spread function (PSF). In other words, individual photons are stochastically recorded on the camera sensor, with a distribution of positions around the actual particle location determined by the PSF⁵³. As a consequence, recording only a few photons will yield a poor estimate of the actual particle position, and the characteristic deviation is determined by the standard error. The latter scales with the inverse root of the number of photons, i.e., for a large number of photons the static localisation error can be as small as a few nanometres⁵⁴. However, for very large numbers of photons, another perturbation becomes visible, the so-called dynamic localisation error: Recording an image to determine a particle’s position takes a finite time during which particles are constantly on the move. As a result, many different positions are visited during the acquisition of a single image and only the temporal mean of these is retrieved from the acquired image as the apparent, particle position. This dynamic localisation error effectively adds a negative offset to $\langle X_t^2 \rangle$ whereas the static localisation error adds a positive offset^{55,56}. Both sources of error will therefore perturb the analysis of the scaling behaviour on short time scales for which experimental trajectories typically yield the best statistics. Thus, determining the value of α and deciding whether diffusional anomalies are present is indeed a major challenge.

The aim of this article is the analysis of a robust and easy-to-implement method that allows one to decide on the type and significance of an apparent anomaly, without being spoiled by localisation errors. We concentrate here on the situation when X_t belongs to a wide, experimentally relevant class of anomalous diffusions—the so-called fractional Brownian motion (FBM)⁵⁷. Note, however, that the methodology we develop here will be amenable to generalisation to any anomalous–diffusion process. FBM is a Gaussian stochastic process characterised by a zero mean value and the covariance function

$$\langle X_{t_1} X_{t_2} \rangle = D \left(t_1^{2H} + t_2^{2H} - |t_1 - t_2|^{2H} \right), \quad (1)$$

where D is a proportionality factor with physical units of length²/time^{2H} commonly referred to as generalised diffusion coefficient and $H \in (0, 1)$ is the traditionally used Hurst index, such that the anomalous diffusion exponent is $\alpha = 2H$. FBM thus describes a process that can be subdiffusive ($H < 1/2$), diffusive ($H = 1/2$), or super-diffusive ($H > 1/2$). From a physical point of view, FBM is well suited to model diffusion in viscoelastic media^{26,27,58–60}, but it also governs observed motion patterns in movement ecology²⁹, the density profiles of serotonergic brain fibres⁶¹, or roughness in financial data⁶².

As mentioned before, localisation errors are usually divided into two kinds of contributions^{55,63}: the static error, due to intrinsic properties of the experimental setup, and the dynamic one, due to the finite time needed for data acquisition, i.e., the exposure time. From a mathematical point of view, the former is generally treated as an independent additive noise source whereas the latter is defined via temporal integration over the finite exposure time. The effect of measurement error in SPT has been investigated mainly by focusing on the MSD^{55,64,65}. Few results are also present in the literature concerning correlation functions and power spectra^{55,56}, but with a small range of applicability. Spectral analysis of stochastic processes can be very helpful in their characterisation, however the power spectrum, according to the textbook definition, is a property that relies on the measurement time going to infinity and on a very large statistical ensemble. Both of these assumptions are typically not met when

dealing with state-of-the-art SPT data, and this is why the spectral analysis of individual trajectories was only recently introduced⁶⁶. The study of single-trajectory spectral densities has been carried out for different stochastic processes^{13,67–72} and is based on the study of the random variable^{66,67}

$$S(f, T) = \frac{1}{T} \left| \int_0^T dt e^{ift} X_t \right|^2 \tag{2}$$

$$= \frac{1}{T} \int_0^T dt_1 \int_0^T dt_2 \cos(f(t_1 - t_2)) X_{t_1} X_{t_2},$$

where f is the frequency, T is the finite observation time, and X_t is an individual realisation of a given stochastic process. We will refer to this quantity as the single-trajectory power spectral density (PSD).

When the parental process X_t is Gaussian, the probability density function (PDF) of the random variable $S(f, T)$ is, likewise, entirely defined by its first moment and variance

$$\mu(f, T) = \langle S(f, T) \rangle, \tag{3}$$

$$\sigma^2(f, T) = \langle S^2(f, T) \rangle - \langle S(f, T) \rangle^2. \tag{4}$$

Note that by taking the limit $\lim_{T \rightarrow \infty} \mu(f, T) = \mu(f)$, we recover the standard definition of the power spectrum. Interestingly it was shown that the characteristic trend of the ensemble-averaged power spectrum $\mu(f, T)$ of several stochastic processes at high frequencies can be inferred already from a single-trajectory PSD^{13,66–71}.

A very interesting quantity to study when performing single-trajectory spectral analyses is the so-called coefficient of variation of the associated PDF, $P(S(f, T))$,

$$\gamma(f, T) = \frac{\sigma(f, T)}{\mu(f, T)}. \tag{5}$$

In particular, when dealing with FBM-like motion the limiting value of $\gamma(f, T)$ at high frequencies (or for a fixed frequency but for long T) turns out to be distinctly different in the cases of subdiffusion ($\gamma(f, T) \sim 1$), normal diffusion ($\gamma(f, T) \sim \sqrt{5}/2$) and superdiffusion ($\gamma(f, T) \sim \sqrt{2}$)⁶⁷. This quantity was proposed in ref. ⁶⁷ as a criterion of anomalous diffusion. Here, we go a significant step further and study how its trend towards specific limiting values is affected by the experimentally unavoidable presence of localisation errors in tracked trajectories. In particular, we show that: (i) this criterion is very robust for subdiffusion; (ii) in the case of superdiffusion the limiting value of $\gamma(f, T)$ is affected by the static measurement error and not by the dynamic error; and (iii) for normal diffusion both static and dynamic errors introduce correction terms in the limiting value of $\gamma(f, T)$. Knowledge of these results allows a reliable determination of the anomalous nature of measured signals.

Results and discussion

As already mentioned above, for pure FBM trajectories it was shown⁶⁷ that the coefficient of variation at high frequencies reaches the limiting values: (i) $\gamma = 1$ for subdiffusion, regardless of the value of H , (ii) $\gamma = \sqrt{5}/2$ for normal diffusion, and (iii) $\gamma = \sqrt{2}$ for superdiffusion, regardless of the value of H . Here, we analyse the case of FBM trajectories in the presence of localisation errors.

Analytical predictions. Let us start by introducing the mathematical description of the two localisation errors:

(i) The static error is usually modelled as an additive noise term, thus we denote with Y_t the joint stochastic process of the

form

$$Y_t = X_t + e_t, \tag{6}$$

where X_t is a pure FBM trajectory and e_t is the static error due to an imperfect measurement. In a standard fashion^{63,64}, we stipulate that e_t is given by the stationary Ornstein–Uhlenbeck (OU) process

$$e_t = \int_{-\infty}^t d\tau e^{-(t-\tau)/\tau_0} \zeta_\tau, \tag{7}$$

where τ_0 is the characteristic relaxation time and ζ_t is a Gaussian white noise with zero mean and covariance $\langle \zeta_t \zeta_{t'} \rangle = 2\sigma_e^2 \delta(t - t')$. Moreover, it is commonly assumed that $\tau_0 \ll \Delta t$, where Δt is the temporal resolution of the trajectory. In other words, we suppose that each time when an instantaneous position X_t is recorded, the latter is specified up to a random “error” with the distribution

$$P(e_t) = \sqrt{\frac{1}{4\pi\sigma_e^2\tau_0}} \exp\left(-\frac{e_t^2}{4\sigma_e^2\tau_0}\right), \tag{8}$$

and is independent of the previous measurements.

(ii) The dynamic error depends on the acquisition or exposure time τ_e , such that the acquired position Y_t can be written as $\bar{X}_t = (1/\tau_e) \int_0^{\tau_e} X_{t-\xi} d\xi$, meaning that we cannot resolve the particle motion below τ_e .

Note that the parameters σ_e and τ_0 for the static error and τ_e for the dynamic error are characteristic of the experimental setup and thus they are usually known quantities when analysing SPT experiments.

As treating the dynamic error within the single-trajectory PSD framework is quite tedious and involved, we limit our analytical study to the joint process (6) in which only the static error is present and leave the dynamic error for numerical study, see “Simulations” subsection in the “Methods” section.

Selecting the process in Eq. (6) and performing the single-trajectory spectral analysis as described above we obtain our central result

$$\gamma_Y^2(f, T) = \frac{\sigma_Y^2(f, T)}{\mu_Y^2(f, T)} = \frac{\sigma_X^2 + \sigma_{OU}^2 + 2\mu_X\mu_{OU}}{(\mu_X + \mu_{OU})^2}, \tag{9}$$

expressing the coefficient of variation of the single-trajectory PSD of the joint process Y_t via the first moments and the variances of the spectral densities of its constituents. In particular, for the OU process under the assumption stated above, we have $\mu_{OU} \sim 2\sigma_e^2\tau_0^2$ and $\sigma_{OU}^2 \sim 4\sigma_e^4\tau_0^4$ (see Supplementary Note 1). The results for the FBM process are dependent on H and are in general quite involved. We report here just the asymptotic trends in the high frequency limit and refer interested readers to ref. ⁶⁷ for more details,

$$H < 1/2 : \mu_X(f, T) \sim \frac{2c_H D}{f^{2H+1}}, \tag{10a}$$

$$H = 1/2 : \mu_X(f, T) \sim \frac{4D}{f^2}, \tag{10b}$$

$$H > 1/2 : \mu_X(f, T) \sim \frac{2D}{f^2} T^{2H-1}, \tag{10c}$$

and $\sigma_X^2(f, T) \sim 4D^2 \left(\frac{c_H^4}{f^{4H+2}} + \frac{2c_H}{f^{2H+3}} T^{2H-1} + \frac{2}{f^4} T^{4H-2} \right)$, where $c_H = \Gamma(2H + 1) \sin(\pi H)$, and $\Gamma(z)$ is the Gamma function⁶⁷. Note that in the case of superdiffusion for fixed T the $1/f^2$ trend could erroneously lead us to the conclusion of having standard diffusion. In addition, the superdiffusive result also shows a

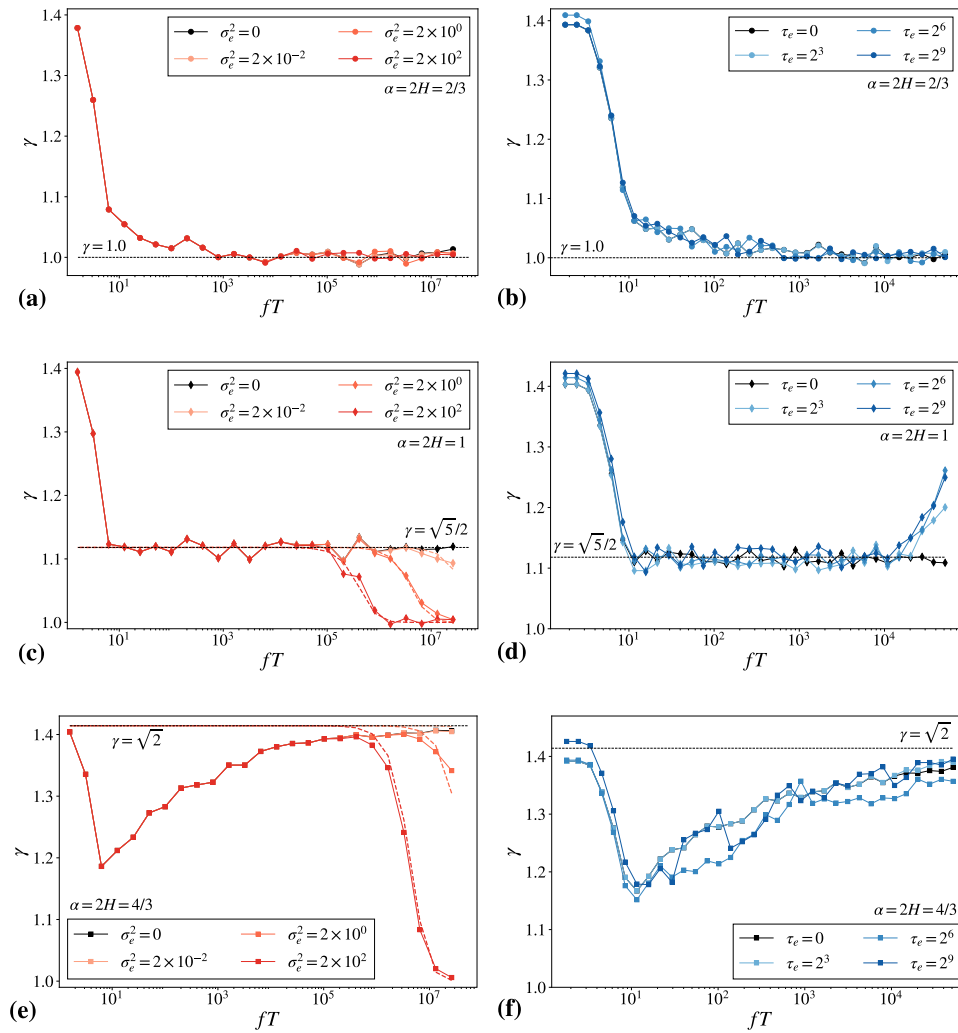


Fig. 1 One-dimensional fractional Brownian motion (FBM) trajectories. We show the coefficient of variation from Monte Carlo simulations of one-dimensional FBM trajectories in the presence of localisation noise. We set the generalised diffusion coefficient to $D = 1$ and the Hurst exponent to **a** and **b** $H = 1/3$ (subdiffusion), **c** and **d** $H = 1/2$ (normal diffusion) and **e** and **f** $H = 2/3$ (superdiffusion). Panels **a**, **c**, and **e**: $n = 10^4$ realisations consisting of $N = 2^{23}$ discrete time steps with $\Delta t = 1$ from the joint process defined in Eq. (6), for static error only. The dashed lines represent the expected high-frequency asymptotic trend reported in Eqs. (11a)–(11c) for the different values of σ_e and $\tau_0 = 1$. Panels **b**, **d**, and **f**: $n = 10^4$ realisations consisting of $N = 2^{14}$ final steps with $\Delta t = 1$ obtained for pure FBM (black) and in the presence of dynamic error with τ_e . The horizontal dashed lines represent the limiting value at high frequencies for pure FBM. Note that γ is reported as a function of fT , thus the limiting values obtained here for high-frequencies are also valid for the case of fixed f and large T .

dependence on T , a clear feature of ageing, that helps in differentiating it from normal diffusion.

The limiting value at high frequencies of the coefficient of variation obtained in Eq. (9) is then given by

$$H < 1/2 : \quad \gamma_Y^2(f, T) \sim 1, \tag{11a}$$

$$H = 1/2 : \quad \gamma_Y^2(f, T) \sim 1 + \frac{1}{4} \left(1 + \frac{\sigma_e^2 \tau_0^2}{2D} f^2 \right)^{-2}, \tag{11b}$$

$$H > 1/2 : \quad \gamma_Y^2(f, T) \sim 1 + \left(1 + \frac{\sigma_e^2 \tau_0^2}{D} \frac{f^2}{T^{2H-1}} \right)^{-2}. \tag{11c}$$

Thus, γ_Y is completely independent of the static noise for subdiffusion, while for normal and superdiffusion correction terms enter. In all of these cases, the limit of zero frequency leads us back to the values in absence of noise, that is $\gamma_Y^2(f = 0) = 2$ (see Supplementary Note 2 for more details). Note that for superdiffusion the limit of long measurement times also leads to the noise-independent value of γ_Y .

Analysis of simulation data. We start our discussion with results from analytical predictions and simulations (see “Analytical predictions” and “Simulations” subsections in the “Methods” section). Results from 1D simulations are shown in Fig. 1. The main goal of this analysis is to elucidate the separate contributions of the two localisation errors, i.e. static and dynamic, in the study of the coefficient of variation γ . Results from simulations in 2D are reported in Fig. 2. The latter are obtained following a procedure that imitates a real experiment (see “Simulations” subsection in the “Methods” section for more details) and thus provide more realistic results to be compared with the ones shown below from experiments.

In Fig. 1, panels a and b we immediately observe that the limiting value of γ in the case of subdiffusive FBM ($H = 1/3$) is not affected by any of the two measurement noises. In the presence of static error only this result was proved also analytically in Eq. (11a).

For the normal diffusive case ($H = 1/2$), in Fig. 1, panels c and d, the situation differs distinctly from the subdiffusive case.

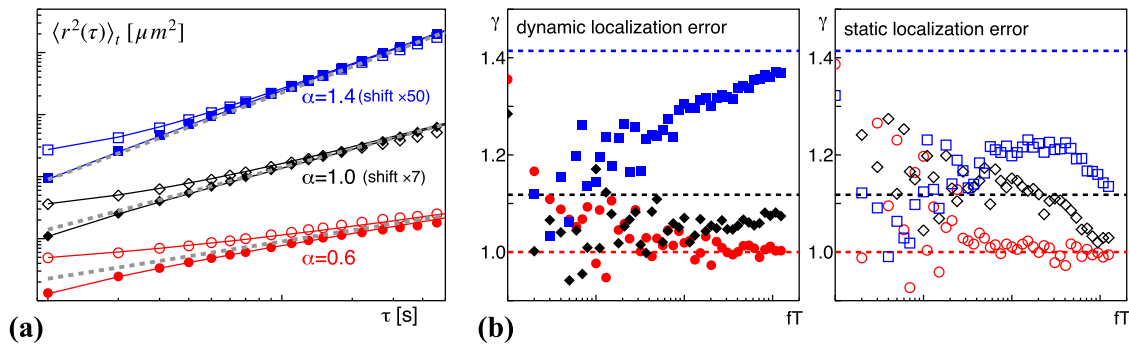


Fig. 2 Two-dimensional fractional Brownian motion (FBM) trajectories. We show the time-averaged mean squared displacements (TA-MSDs) and the coefficient of variation from Monte Carlo simulations of two-dimensional FBM trajectories in the presence of localisation noise. **a** Representative time-averaged mean squared displacements (TA-MSDs) of individual two-dimensional FBM trajectories created with $H = 0.3$ (red circles), $H = 0.5$ (black diamonds), and $H = 0.7$ (blue squares) follow the anticipated power-law scaling (grey dashed lines) for sufficiently long lag times τ . Ensemble averages of TA-MSDs are superimposed as coloured full lines. For short lag times, significant deviations due to a dominant dynamic localisation error ($n_p = 900$, filled symbols) or a dominant static localisation error ($n_p = 50$, open symbols) are visible. These may significantly perturb the extraction of the TA-MSD's scaling exponent, $\alpha = 2H$. **b** The coefficient of variation γ , for the case of a dominant dynamic localisation error (filled symbols) converges towards the predicted values $\gamma = 1$, $\sqrt{5}/2$ and $\sqrt{2}$ (highlighted by the coloured dashed lines). While the subdiffusive case (red) converges rapidly, normal diffusion and superdiffusion (black and blue, respectively) may need longer trajectories to eventually reach the predicted value. In contrast, for a dominant static localisation error (open symbols) only the subdiffusive case (red) is in agreement with the predicted value $\gamma = 1$ whereas normal diffusion and superdiffusion (black and blue) are very sensitive to this perturbation.

Namely, the limiting value of γ is affected by both types of measurement noise, resulting in two opposite effects. On the one hand, the static localisation error leads to a drop in the value of γ (Fig. 1, panel c). In particular, from the analytical result Eq. (11b) one can see that when the ratio σ_e^2/D grows, γ decreases, approaching the new limiting value $\gamma = 1$ at very high frequencies. On the other hand, from our numerical study in Fig. 1, panel d one can see that the dynamic localisation error causes an increase in the limiting value of γ . The greater τ_e the smaller the value of fT at which we observe a deviation from the pure value $\gamma = \sqrt{5}/2$.

For superdiffusive FBM, the results are reported in Fig. 1, panels e and f, showing that the limiting value of γ is mostly affected by the presence of static localisation errors. The latter, similarly to the diffusive case, leads to a drop in the limiting value of γ . In particular, if we look at the explicit analytic expression reported in Eq. (11c) we see that upon increasing the ratio σ_e^2/D the coefficient of variation drops, until it reaches the new limiting value $\gamma = 1$, as for BM ($\alpha = 1$). Moreover, in this case, the trajectory length T also turns out to be a key parameter in determining the final trend of γ : for very long trajectories the presence of static measurement noise becomes less and less influential. For the dynamic error instead, we see from Fig. 1, panel (f) that, regardless of the value of τ_e , the trend of γ does not present any relevant change.

In general, we observe that localisation errors affect the trend of γ for normal diffusion and superdiffusive FBM only. For both cases ($\alpha = 1$ and $\alpha > 1$), when the variance σ_e of the static error increases, the drop of γ to the ultimate value 1 occurs at progressively lower values of fT . Instead, when changing the key parameter of the dynamic error (τ_e), the trend of γ is affected only in the case of normal diffusion, showing an increase in its limiting value.

The analysis of numerically obtained FBM data in 2D with different localisation errors is reported in Fig. 2. As can be seen, these results agree with the discussion for the case of the 1D simulations. On the one hand, in the case of subdiffusive FBM the coefficient of variation is insensitive to any of the localisation errors, always converging to the prediction $\gamma = 1$. Therefore, this

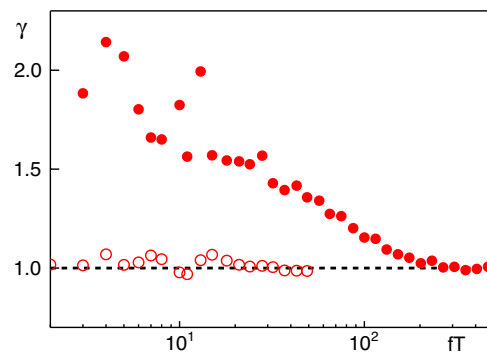


Fig. 3 Coefficient of variation obtained from experimental subdiffusive trajectories with a marked anti-persistence. Results from two datasets are shown: experimental tracking of p-granules in *C. elegans* embryos (open red circles) and telomeres in the nucleus of mammalian culture cells (filled red circles). They both comply with the expectation for subdiffusive data that γ converges to unity (indicated by the black dashed line). In both cases, the MSDs contained a non-negligible static localisation error.

measure is a very robust means to explore whether tracking data indeed show a subdiffusive behaviour. On the other hand, diffusive and superdiffusive FBM data do not appear to be very sensitive to the presence of dynamic noise, but their results change dramatically when static noise is present, causing a clear drop in the value of γ at high frequencies.

Analysis of experimental data. Analytical and numerical results are nicely confirmed by the analysis of experimental data. Figure 3 shows results from subdiffusive tracking data on (i) telomeres in the nucleus of mammalian culture cells⁷³, and (ii) p-granules in the cytoplasm of *C. elegans* embryos⁷⁴, all distinctly displaying a convergence to $\gamma = 1$, fully consistent with our predictions.

Experimental data obtained by tracking the motion of beads in water, reported in Fig. 4, show some nice results for the normal-diffusion regime. For the pure experimental data (base-line) we can see an increase in the value of γ at high frequencies. We

showed that this deviation from the expected value is due to the effect of the dynamic error. Moreover, if in a post-analysis we artificially increase the static localisation error, we observe that the value of γ starts decreasing upon the increase of σ_s , approaching the new limiting value $\gamma = 1$ (red dashed line in Fig. 4). These observations are fully in line with our predictions.

We now move to the analysis of superdiffusive experimental data. Cytoskeleton fluctuations were measured by attaching RGD-coated beads to the surface of human alveolar epithelial cells (see the sketch in Fig. 5, panel a). The beads were connected to the actin cytoskeleton and rearranged by internal molecular motors. Given that molecular motor activity depends on temperature, the data show a marked superdiffusive behaviour at high temperatures ($\geq 29^\circ\text{C}$, green triangles and blue circles in Fig. 5, panel b). Interestingly, at low temperatures ($\leq 21^\circ\text{C}$) the data show that cytoskeleton fluctuations transition from a subdiffusive behaviour at short timescales to a superdiffusive behaviour at longer timescales (black squares in Fig. 5, panel b). This crossover can be explained by the Arrhenius dependence of the activity of molecular motors on temperature⁷⁵. Using the coefficient of variation γ to assess the diffusion regime, we observe that cytoskeletal fluctuations obtained at high temperatures (29 and 37°C) display a robust superdiffusive behaviour at

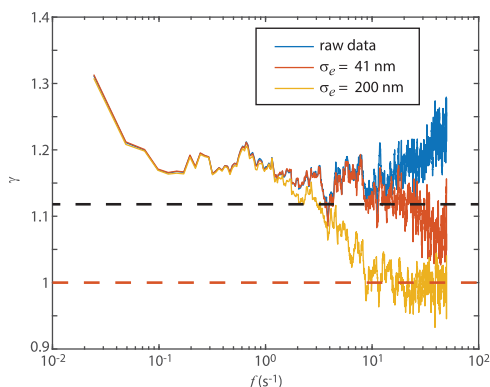


Fig. 4 Coefficient of variation obtained from diffusive data of beads in water. The baseline is marked in blue. Static localisation errors are artificially added to the data to obtain the other two curves. The red and black dashed lines indicate $\gamma = 1$ and $\sqrt{5}/2$, respectively, which are the values to which γ converges in the case of subdiffusion and normal diffusion when no error is present.

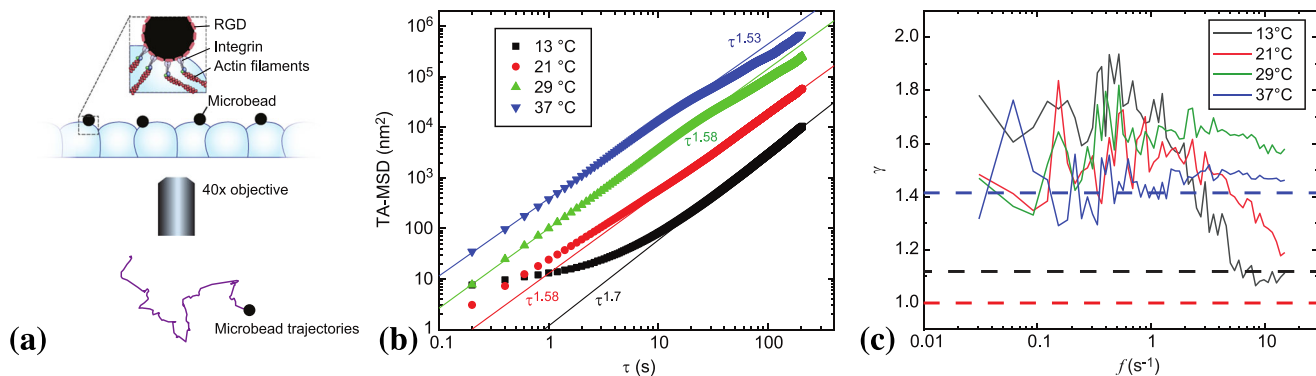


Fig. 5 Cytoskeleton fluctuations of living cells exhibit superdiffusive behaviour. **a** Sketch of the experimental system for microbeads attached to the surface of epithelial cells (see the “Experiments” subsection in the “Methods” section for more details) together with a representative experimental trajectory. **b** MSD at varying temperatures. The straight lines show that the dynamics are superdiffusive with $2H$ between 1.5 and 1.7, depending on temperature. **c** Coefficient of variation of the power spectrum of the motion of the surface-bound microbeads. The dashed lines indicate $\gamma = 1$, $\sqrt{5}/2$, and $\sqrt{2}$, the predicted limiting values of γ for the different diffusion regimes, in the absence of any noise.

all different timescales. The subdiffusive to superdiffusive crossover at 13 and 21°C is well captured as γ approaches 1 for frequencies >20 rad/s (Fig. 5, panel c). At longer timescales the value of γ indicates superdiffusive behaviour, showing that at low temperatures, molecular motors are active at longer timescales. From the analysis of this dataset, we can draw two conclusions. First, we see that there is no statistically relevant effect due to localisation errors. Second, we observe that the value of γ is very sensitive to crossovers between different diffusive regimes, confirming that this quantity is useful for the statistical analysis of experimental data.

Finally, we consider the diffusion of nanoparticles in the cytoplasm of human Mesenchymal stem cells. In Fig. 6 panel a, we report the MSD showing a mildly superdiffusive ($\alpha = 1.23$) regime, in agreement with the fact that the nanoparticles are embedded into the active intracellular environment. However, the MSD trend is strongly affected by the presence of the static localisation error, making the fit less reliable. By calculating the coefficient of variation, reported in Fig. 6, panel b, we clearly confirm the superdiffusive trend, as γ converges nicely to the analytical value for the superdiffusion regime, that is $\sqrt{2}$, without displaying large deviations due to the static error.

Conclusions

Departures from the Brownian behaviour of diffusive processes are observed in a wide variety of systems of practical interest across many disciplines, and these phenomena call for explanations and understanding of the underlying physical processes and microscopic mechanisms. Without such knowledge, one cannot fully comprehend and reach a full picture of the phenomena. Concurrently, a conclusion that the dynamics are indeed anomalous relies on proper data treatment, the size of statistical samples, blurring measurement errors and errors incurred by the fitting procedures, or transients obscuring the true scaling exponents. It is therefore indispensable to have at hand robust methods allowing one to reach justified, sound conclusions on the dynamics.

In this work, we test the coefficient of variation γ of the single-trajectory power spectral density and show that it represents a valuable method towards a robust criterion for anomalous diffusion. We combine analytical, numerical and experimental studies of diffusive dynamics in very diverse systems, to demonstrate how the values of γ for trajectories belonging to FBM are affected by the presence of localisation errors. Within such a combined effort, numerical simulations which imitate real experiments

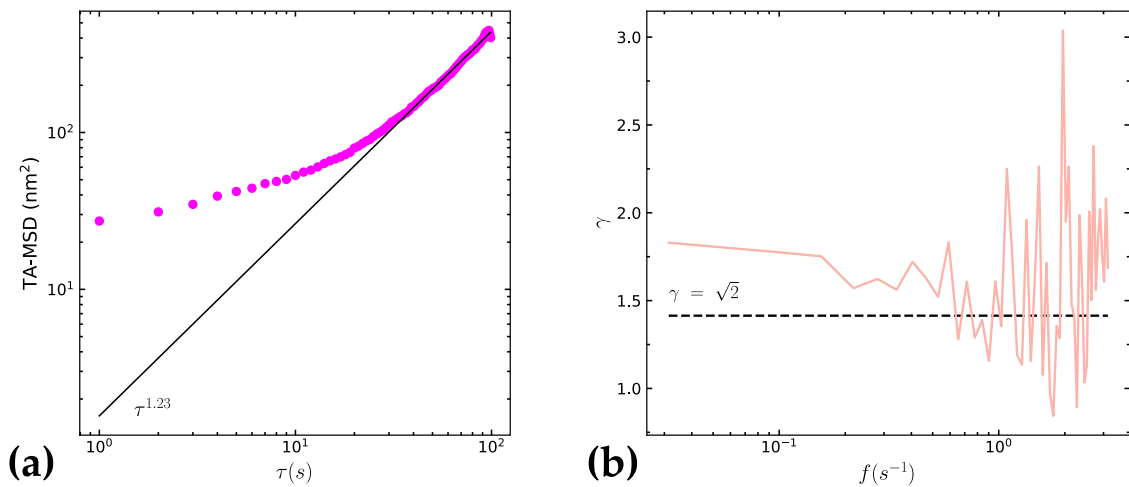


Fig. 6 Mean squared displacement (MSD) and coefficient of variation for superdiffusive nanoparticles in hMSCs. **a** MSD showing a superdiffusive regime with large deviations due to the presence of the static localisation error. **b** The coefficient of variation confirms the superdiffusive trend.

performed here serve us to elucidate the relative contributions of static and dynamic measurement noise in a controllable way, and therefore to prove our theoretical results and concepts. A further comparison with experimental data obtained for rather diverse systems permits us to verify the predicted trends and thus obtain a fully comprehensive picture.

Apart from the case $f \rightarrow 0$ in which the coefficient of variation $\gamma(f, T)$ converges to the universal value $\sqrt{2}$, we found that our results vary depending on the specific diffusive regime and on the kind of localisation error. In particular, the coefficient of variation represents a very robust way to define whether tracking data show a subdiffusive behaviour. This can be of decisive help in data analysis, in particular, when the deviation of the anomalous exponent from unity is small and thus the fitting of the MSD can produce misleading results. Conversely, diffusive and superdiffusive data are more sensitive to measurement noise. In these regimes the value of γ displays a clear drop at high frequencies in the presence of a static localisation error, which is corroborated by both numerical and experimental data, while the effect of a dynamic error appears to be relevant for the normal-diffusive regime only, causing an increase in the limiting value of γ at high frequencies. As well, this theoretical prediction is confirmed by our numerical and experimental results. Thus, in the case of superdiffusion the criterion remains very robust in the presence of dynamic error while in general, it is not when static localisation error is present. Nevertheless, the analytical expression obtained for the correction term still allows us to control the effect of the measurement error in this case. Finally, the criterion appears to be the least robust for normal diffusion, which is affected by both static and dynamic localisation errors. Arguably, the observed trends in γ can be used also to post-process the data by adding static and dynamic errors to explore the limiting values of γ as a function of noise intensity.

The application of our method to diverse experimental systems presented in our paper evidence that it provides a very robust tool for the analysis of the anomalous character of random motion. In conjunction with the MSD analysis, it will permit to make of conclusive statements on the actual departures from standard diffusive motion, even in the presence of unavoidable errors in experimental measurements, and thus point towards the necessity to understand the actual underlying physical mechanisms. Apart from a stand-alone criterion, our power spectral method will also represent an important ingredient in decision trees and feature-based neural network approaches.

Methods

Simulation methods. We perform simulations of FBM trajectories in 1D and 2D in order to complement and support our analytical predictions as well as the analysis of experimental data. The simulations are performed in Python for the 1D case and in Matlab for the 2D case.

1D case. FBM trajectories of length $T = N \times \Delta t$, where N corresponds to the total number of time steps and Δt to the discretisation time step, are generated for different values of the Hurst index H to explore all three regimes via the *fbm* package in Python. In order to include the dynamic error, given a fixed exposure time τ_e corresponding to $n_e = \tau_e / \Delta t$ time steps, we first simulate longer FBM trajectories with a total number $N_e = N \times n_e$ of time steps. Then, from each of these trajectories, a new trajectory is obtained, whose points are given by the average over n_e subpoints of the original trajectory, i.e., $\bar{X}(t_i) = \frac{1}{n_e} \sum_{j=0}^{n_e-1} X(t_i - j\Delta t)$. As far as the static error is concerned we use its definition (7) and generate stationary OU trajectories with relaxation time $\tau_0 = \Delta t$ and varying noise amplitude σ_e .

2D case. An ensemble of $M = 100$ two-dimensional FBM trajectories, each with $N = 2500$ positions covering a total time $T = N \times \Delta t$ with $\Delta t = 0.1$ s was created with the Matlab routine *wfbm* for the Hurst coefficients $H = 0.3, 0.5$, and 0.7 , hence exploring FBM from the subdiffusive to the superdiffusive regimes. Mean step sizes within Δt along each coordinate were chosen to be $0.01 \mu\text{m}$. To account for the dynamic and static localisation errors, each time step was subdivided into $n_e = 10$ substeps during each of which n_p positions according to a diffraction-limited Gaussian PSF, centred at the particle position at that time, were calculated. To this end, initial FBM tracks had a length $i = 1, \dots, Nn_e$ and at each substep location x_p , a total of $j = 1, \dots, n_p$ positions $x_{i,j} = x_i + \xi_j$ were produced, where ξ_j are Gaussian random numbers with zero mean and standard deviation $\sigma = 0.220 \mu\text{m}$. From this, track positions were determined via

$$X_k = X(k\Delta t) = \frac{1}{n_e n_p} \sum_{i=(k-1)n_e+1}^{kn_e} \sum_{j=1}^{n_p} x_{i,j}. \quad (12)$$

For $n_p < 100$, this procedure creates a dominant static localisation error whereas for $n_p \gg 100$ only a dynamic localisation error is seen.

Experimental systems. To assess the applicability of experimental data of the coefficient of variation analysis in the presence of localisation errors, we analysed experimental data displaying different diffusive regimes. In what follows we report a short description of the experimental systems.

Subdiffusive data

Experimental tracking data for p-granules in *C. elegans* embryos: The data were obtained and analysed as described in ref. 74. As shown before, p-granule trajectories have a noticeable static localisation error that perturbs, e.g., the velocity autocorrelation function. Here, only trajectories with $N = 100$ positions at a time increment $\Delta t = 210$ ms with a subdiffusive TA-MSD scaling were considered. Trajectories with scaling exponents $\alpha \in [0.7, 0.9]$, $\alpha \in [0.5, 0.7]$, and $\alpha \in [0.3, 0.5]$ were grouped into three distinct sets. For each, γ was calculated as a function of fT , and the average of these was used for Fig. 3 to soften fluctuations induced by the fairly short trajectories.

Trajectories for telomeres in the nucleus of mammalian culture cells: The data were obtained similar to our previous work⁷³: U2OS cells (DSMZ Cat# ACC-785,

RRID:CVCL_0042) were cultured as described and telomeres were highlighted by transient transfection with a plasmid for GFP-tagged TRF-2 (24 h prior to microscopy, using Lipofectamine3000 according to the manufacturer's protocol). For live-cell microscopy, cells were plated 24 h prior to transfection in four-well μ -slide microscopy chambers; 15 min prior to imaging, the medium was changed to MEM without phenol red supplemented with 5% FCS and 5% HEPES. Imaging was performed with a customised spinning-disk confocal microscope based on a DMI 4000 stand (Leica Microsystems, Germany) with a custom-made incubation chamber, a CSU-X1 spinning-disk unit (Yokogawa Microsystems, Japan), an HC PL APO $\times 100/1.40NA$ oil immersion objective, and an Evolve 512 EMCCD camera (Photometrics, USA). Samples were illuminated at 488 nm and fluorescence was detected in the range 500–550 nm. Trajectories were recorded at a time increment $\Delta t = 110$ ms and only trajectories with at least $N = 1000$ positions were retained (and trimmed to the same length if trajectories were longer). In line with our previous finding, trajectories featured an anti-persistent subdiffusion with an average scaling exponent of $\alpha \approx 0.55$.

In both cases, the generalised diffusion coefficients of individual trajectories varied log-normally. To soften the influence of this locus- and particle-dependent prefactor in the PSD analysis, each trajectory was normalised in each coordinate by its respective root-mean-squared step taken within Δt before calculating γ .

Diffusive data. We analysed the motion of 1.2 μm -sized polystyrene beads in aqueous solution as representative experimental data for Brownian motion. Namely, we suspended the beads in phosphate-buffered saline with 1% bovine serum albumin and 0.05% Tween 20 to avoid the aggregation and introduced the suspension into a flow cell chamber. Subsequently, the flow cell chamber was sealed for imaging. The beads were imaged at 100 frames per second in an inverted microscope with a $\times 40$ objective (Olympus PlanApo, N.A. 0.95) and a sCMOS camera (Andor Zyla 4.2). Bead tracking in the plane was performed in LabView using a cross-correlation-based tracking algorithm. A set of 150 trajectories, each consisting of 4096 frames, was used in the analysis.

Superdiffusive data

Cytoskeleton fluctuations of living cells at different temperatures⁷⁵. Cytoskeleton fluctuations were measured by tracking the trajectory of refractive microbeads attached to the surface of human alveolar epithelial cells (A549). The microbeads were previously coated with Arginine–Glycine–Aspartic acid (RGD) containing peptide (Peptide 2000, Integra Life Sciences, San Diego, CA) to link the probe to the actin cytoskeleton through integrin membrane receptors. The movement of these beads was sensitive to a wide range of cytoskeleton manipulations including actin polymerisation/depolymerisation drugs, actomyosin relaxation, cell stretching, temperature changes, and ATP depletion⁷⁶ indicating that spatial fluctuations of microbeads linked to integrin membrane receptors reflect intrinsic cytoskeleton dynamics.

Microbead positions were tracked at $\times 40$ magnification using an inverted microscope (TE-2000E, Nikon, Japan) equipped with a charge-coupled device (CCD) camera (Orca, Hamamatsu, Japan). The spontaneous microbead movement was tracked for 200–400 s at a sampling rate of 5 Hz. The position of the microbead was determined with subpixel resolution by computing the microbead centroid with an intensity-weighted average algorithm implemented with custom-made software (LABVIEW, National Instruments, USA). Data were corrected for the drift of the stage of the microscope, which was computed as the average change in the position of all microbeads within the field of view.

The temperature dependence of cytoskeleton fluctuations was measured by heating or cooling the microscope stage with a microincubator system (HCMIS MicroIncubator System, ALA Science, Westbury, NY) and closed-loop control. The sample temperature was measured with a negative temperature coefficient thermistor (332 Temperature Controller, Lakeshore, Westerville, OH). Measurements were taken in $n = 6$ wells (~ 20 microbead/well) per temperature.

Human alveolar epithelial cells (A549) (cell line CCL-185 ATCC, Manassas, VA) were cultured in RPMI 1640 medium supplemented with 1 mM L-glutamine, 100 U/ml penicillin, 100 mg/ml streptomycin and 2 $\mu\text{g}/\text{ml}$ amphoterin B (all from GIBCO, Gaithersburg, MD), 10% inactivated fetal calf serum (Biological Industries, Kibbutz Beit Haemek, Israel), and buffered with HEPES (Sigma, St. Louis, MO). One day before experiments cells were harvested with brief exposure to trypsin-EDTA (Sigma) and plated (900 cells/ mm^2) on collagen-coated wells.

Diffusion of nanoparticles in the cytoplasm of human Mesenchymal stem cells: Here we tracked yellow-green fluorospheres of size 100 nm injected carefully in the cytoplasm of human mesenchymal stem cells (hMSCs). The fluorospheres (FluoSpheres™ ThermoFisher, Cat. No. F8803) were negatively charged (carboxylated-modified) polystyrene beads that are suitable for intracellular tracking. Samples were prepared by diluting the suspension to 2 mg/ml concentration after 20 min sonication of the stock solution to ensure even dispersion of the particles in the solution. The diluted solution subsequently was vortexed for 2 min for optimised mixing and then loaded via a microloader pipette (Eppendorf) in manufactured glass capillaries appropriate for microinjection (FemtoTIPS™ Eppendorf Cat. No. 5242952008). Their microinjection was executed at room temperature using a micromanipulation system (Eppendorf) at controlled pressure. Immediately after the injection, imaging was performed 100 s at room temperature with an Olympus IX81 inverted microscope using an Olympus UPLSAPO $\times 40/0.95$ Objective and a Hamamatsu Orca-2 camera. At each

frame of the resulting video files, the particles were identified and their movement was tracked using a publicly available Python package which also provides tools to spot the candidate features based on high-intensity matches, filtering and different type of corrections such as drift correction⁷⁷.

Data availability

The data reported in this work are available from the corresponding authors upon reasonable request.

Code availability

The codes used to obtain the results of this work are available from the corresponding authors upon reasonable request.

Received: 27 May 2022; Accepted: 8 November 2022;

Published online: 28 November 2022

References

- Zia, R. N. Active and passive microrheology: theory and simulation. *Annu. Rev. Fluid Mech.* **50**, 371–405 (2018).
- Shen, H. et al. Single particle tracking: from theory to biophysical applications. *Chem. Rev.* **117**, 7331–7376 (2017).
- Manzo, C. & Garcia-Parajo, M. F. A review of progress in single particle tracking: from methods to biophysical insights. *Rep. Prog. Phys.* **78**, 124601 (2015).
- Mogre, S. S., Brown, A. I. & Koslover, E. F. Getting around the cell: physical transport in the intracellular world. *Phys. Biol.* **17**, 061003 (2020).
- Golding, I. & Cox, E. C. Physical nature of bacterial cytoplasm. *Phys. Rev. Lett.* **96**, 098102 (2006).
- Barkai, E., Garini, Y. & Metzler, R. Strange kinetics of single molecules in living cells. *Phys. Today* **65**, 29 (2012).
- Metzler, R., Jeon, J. H., Cherstvy, A. G. & Barkai, E. Anomalous diffusion models and their properties: non-stationarity, non-ergodicity, and ageing at the centenary of single particle tracking. *Phys. Chem. Chem. Phys.* **16**, 24128 (2014).
- Nørregaard, K., Metzler, R., Ritter, C. M., Berg-Sørensen, K. & Oddershede, L. B. Manipulation and motion of organelles and single molecules in living cells. *Chem. Rev.* **117**, 4342 (2017).
- Krapf, D. & Metzler, R. Strange interfacial molecular dynamics. *Phys. Today* **72**, 48 (2019).
- Seisenberger, G. et al. Real-time single-molecule imaging of the infection pathway of an adeno-associated virus. *Science* **294**, 1929 (2001).
- He, W. et al. Dynamic heterogeneity and non-Gaussian statistics for acetylcholine receptors on live cell membrane. *Nat. Commun.* **7**, 11701 (2016).
- Platani, M., Goldberg, L., Lamond, A. I. & Swedlow, J. R. Cajal body dynamics and association with chromatin are ATP-dependent. *Nat. Cell Biol.* **4**, 502 (2002).
- Fox, Z. R., Barkai, E. & Krapf, D. Aging power spectrum of membrane protein transport and other subordinated random walks. *Nat. Commun.* **12**, 6162 (2021).
- Etoc, F. et al. Non-specific interactions govern cytosolic diffusion of nanosized objects in mammalian cells. *Nat. Mater.* **17**, 740 (2018).
- Song, M. S., Moon, H. C., Jeon, J.-H. & Park, H. Y. Neuronal messenger ribonucleoprotein transport follows an aging Lévy walk. *Nat. Commun.* **9**, 344 (2018).
- Sungkaworn, T. et al. Single-molecule imaging reveals receptor-G protein interactions at cell surface hot spots. *Nature* **550**, 543 (2017).
- Ramm, B. et al. A diffusophoretic mechanism for ATP-driven transport without motor proteins. *Nat. Phys.* **17**, 850 (2021).
- Normanno, D. et al. Probing the target search of DNA-binding proteins in mammalian cells using TetR as model searcher. *Nat. Commun.* **6**, 7357 (2015).
- Heller, I. et al. STED nanoscopy combined with optical tweezers reveals protein dynamics on densely covered DNA. *Nat. Methods* **10**, 910 (2013).
- Di Rienzo, C., Piazza, V., Gratton, E., Beltram, F. & Cardarelli, F. Probing short-range protein Brownian motion in the cytoplasm of living cells. *Nat. Commun.* **5**, 5891 (2014).
- Golan, Y. & Sherman, E. Resolving mixed mechanisms of protein subdiffusion at the T cell plasma membrane. *Nat. Commun.* **8**, 15851 (2017).
- Thompson, M. A., Casolari, J. M., Badiestrom, M., Brown, P. O. & Moerner, W. E. Three-dimensional tracking of single mRNA particles in *Saccharomyces cerevisiae* using a double-helix point spread function. *Proc. Natl Acad. Sci. USA* **107**, 17864 (2010).

23. Chen, K., Wang, B. & Granick, S. Memoryless self-reinforcing directionality in endosomal active transport within living cells. *Nat. Mater.* **14**, 589 (2015).
24. Tabei, S. M. A. et al. Intracellular transport of insulin granules is a subordinated random walk. *Proc. Natl Acad. Sci. USA* **110**, 4911 (2013).
25. Bronstein, I. et al. Transient anomalous diffusion of telomeres in the nucleus of mammalian cells. *Phys. Rev. Lett.* **103**, 018102 (2009).
26. Weber, S. C., Spakowitz, A. J. & Theriot, J. A. Bacterial chromosomal loci move subdiffusively through a viscoelastic cytoplasm. *Phys. Rev. Lett.* **104**, 238102 (2010).
27. Jeon, J.-H. et al. In vivo anomalous diffusion and weak ergodicity breaking of lipid granules. *Phys. Rev. Lett.* **106**, 048103 (2011).
28. Thapa, S., Lukat, N., Selhuber-Unkel, C., Cherstvy, A. G. & Metzler, R. Transient superdiffusion of polydisperse vacuoles inside highly-motile amoeboid cells. *J. Chem. Phys.* **150**, 144901 (2019).
29. Vilks, O. et al. Unravelling the origins of anomalous diffusion: from molecules to migrating storks. *Phys. Rev. Res.* **4**, 033055 (2022).
30. Nathan, R. et al. Big-data approaches lead to an increased understanding of the ecology of animal movement. *Science* **375**, eabg1780 (2022).
31. Erickson, A. M., Henry, B. I., Murray, J. M., Klasse, P. J. & Angstmann, C. N. Predicting first traversal times for virions and nanoparticles in mucus with slowed diffusion. *Biophys. J.* **109**, 164 (2015).
32. Bronshtein, I. et al. Loss of lamin A function increases chromatin dynamics in the nuclear interior. *Nature Communications* **6**, 8044 (2015).
33. Vilks, O. et al. Ergodicity breaking in area-restricted search of Avian predators. *Phys. Rev. X* **12**, 031005 (2022).
34. Bräuchle, C., Lamb, D. C. & Michaelis, J. *Single Particle Tracking and Single Molecule Energy Transfer* (Wiley-VCH, Weinheim, Germany, 2012).
35. Martin, D. S., Forstner, M. B. & Käs, J. A. Apparent subdiffusion inherent to single particle tracking. *Biophys. J.* **83**, 2109 (2002).
36. Tejedor, V. et al. Quantitative analysis of single particle trajectories: mean maximal excursion method. *Biophys. J.* **98**, 1364 (2010).
37. Thapa, S., Lomholt, M. A., Krog, J., Cherstvy, A. G. & Metzler, R. Bayesian analysis of single-particle tracking data using the nested-sampling algorithm: maximum-likelihood model selection applied to stochastic-diffusivity data. *Phys. Chem. Chem. Phys.* **20**, 29018 (2018).
38. Cherstvy, A. G., Thapa, S., Wagner, C. E. & Metzler, R. Non-Gaussian, non-ergodic, and non-Fickian diffusion of tracers in mucin hydrogels. *Soft Matter* **15**, 2526 (2019).
39. Krog, J., Jacobsen, L. H., Lund, F. W., Wüstner, D. & Lomholt, M. A. Bayesian model selection with fractional Brownian motion. *J. Stat. Mech.* **2018**, 093501 (2018).
40. Muñoz-Gil, G., Garcia-March, M. A., Manzo, C., Martín-Guerrero, J. D. & Lewenstein, M. Single trajectory characterization via machine learning. *N. J. Phys.* **22**, 013010 (2020).
41. Granik, N. et al. Single-particle diffusion characterization by deep learning. *Biophys. J.* **117**, 185 (2019).
42. Kowalek, P., Loch-Olzsewska, H. & Szwabiński, J. Classification of diffusion modes in single-particle tracking data: feature-based versus deep-learning approach. *Phys. Rev. E* **100**, 032410 (2019).
43. Loch-Olzsewska, H. & Szwabiński, J. Impact of feature choice on machine learning classification of fractional anomalous diffusion. *Entropy* **22**, e22121436 (2020).
44. Muñoz-Gil, G. et al. Objective comparison of methods to decode anomalous diffusion. *Nat. Commun.* **12**, 6253 (2021).
45. Seckler, H. & Ralf, M. Bayesian deep learning for error estimation in the analysis of anomalous diffusion. *Nature Communications* **13**, 6717 (2022).
46. Díez Fernandez, A., Charchar, P., Cherstvy, A. G., Metzler, R. & Finnis, M. W. The diffusion of doxorubicin drug molecules in silica nanoslits is non-Gaussian, intermittent and anticorrelated. *Phys. Chem. Chem. Phys.* **22**, 27955 (2020).
47. Ślęzak, J., Burnecki, K. & Metzler, R. Random coefficient autoregressive processes describe Brownian yet non-Gaussian diffusion in heterogeneous systems. *N. J. Phys.* **21**, 073056 (2019).
48. Boyer, D., Dean, D. S., Mejía-Monasterio, C. & Oshanin, G. Optimal estimates of the diffusion coefficient of a single Brownian trajectory, *Phys. Rev. E* **85**, 031136 (2012); Distribution of the least-squares estimators of a single Brownian trajectory diffusion coefficient. *J. Stat. Mech. Theor. Exp.* **2013**, P04017 (2013).
49. Vestergaard, C. L., Blainey, P. C. & Flyvbjerg, H. Optimal estimation of diffusion coefficients from single-particle trajectories. *Phys. Rev. E* **89**, 022726 (2014).
50. Chakraborty, I. & Roichman, Y. Disorder-induced Fickian, yet non-Gaussian diffusion in heterogeneous media. *Phys. Rev. Res.* **2**, 022020(R) (2020).
51. Lanoiselée, Y., Moutal, N. & Grebenkov, D. S. Diffusion-limited reactions in dynamic heterogeneous media. *Nat. Commun.* **9**, 4398 (2018).
52. Han, D. et al. Deciphering anomalous heterogeneous intracellular transport with neural networks. *eLife* **9**, e52224 (2020).
53. Ober, R. J., Ram, S. & Ward, E. S. Localization accuracy in single-molecule microscopy. *Biophys. J.* **86**, 1185 (2004).
54. Yildiz, A. & Selvin, P. R. Fluorescence imaging with one nanometer accuracy: application to molecular motors. *Acc. Chem. Res.* **38**, 574 (2005).
55. Savin, T. & Doyle, P. S. Static and dynamic error in particle tracking microrheology. *Biophys. J.* **88**, 623 (2005).
56. Backlund, M. P., Joyner, R. & Moerner, W. Chromosomal locus tracking with proper accounting of static and dynamic errors. *Phys. Rev. E* **91**, 062716 (2015).
57. Mandelbrot, B. B. & Van Ness, J. W. Fractional Brownian motions, fractional noises and applications. *SIAM Rev.* **10**, 422 (1968).
58. Guigas, G., Kalla, V. & Weiss, M. Probing the nanoscale viscoelasticity of intracellular fluids in living cells. *Biophys. J.* **93**, 316 (2007).
59. Jeon, J.-H., Leijnse, N., Oddershede, L. & Metzler, R. Anomalous diffusion and power-law relaxation of the time averaged mean squared displacement in worm-like micellar solutions. *N. J. Phys.* **15**, 045011 (2013).
60. Magdziarz, M., Weron, A., Burnecki, K. & Klafter, J. Fractional Brownian motion versus the continuous-time random walk: a simple test for subdiffusive dynamics. *Phys. Rev. Lett.* **103**, 180602 (2009).
61. Janušonis, S., Detering, N., Metzler, R. & Vojta, T. Serotonergic axons as fractional brownian motion paths: insights into the self-organization of regional densities. *Front. Comp. Neurosci.* **14**, 56 (2020).
62. Beran, J., Feng, Y., Ghosh, S. & Kulik, R. *Long-memory Processes* (Springer, Berlin, 2016).
63. Berglund, A. Statistics of camera-based single-particle tracking. *Phys. Rev. E* **82**, 011917 (2010).
64. Michalet, X. Mean square displacement analysis of single-particle trajectories with localization error: Brownian motion in an isotropic medium. *Phys. Rev. E* **82**, 041914 (2010).
65. Weiss, M. Resampling single-particle tracking data eliminates localization errors and reveals proper diffusion anomalies. *Phys. Rev. E* **100**, 042125 (2019).
66. Krapf, D. et al. Power spectral density of a single Brownian trajectory: what one can and cannot learn from it. *N. J. Phys.* **20**, 023029 (2018).
67. Krapf, D. et al. Spectral content of a single non-Brownian trajectory. *Phys. Rev. X* **9**, 011019 (2019).
68. Sposini, V., Metzler, R. & Oshanin, G. Single-trajectory spectral analysis of scaled Brownian motion. *N. J. Phys.* **21**, 073043 (2019).
69. Sposini, V., Grebenkov, D. S., Metzler, R., Oshanin, G. & Seno, F. Universal spectral features of different classes of random diffusivity processes. *N. J. Phys.* **22**, 063056 (2020).
70. Squarcini, A., Solon, A. & Oshanin, G. Spectral density of individual trajectories of an active Brownian particle. *N. J. Phys.* **24**, 013018 (2022).
71. Cerasoli, S. et al. Spectral fingerprints of non-equilibrium dynamics: The case of a Brownian gyrator. *Phys. Rev. E* **106**, 014137 (2022).
72. Vilks, O. et al. Classification of anomalous diffusion in animal movement data using power spectral analysis. *J. Phys. A: Math. Theor.* **55**, 334004 (2022).
73. Stadler, L. & Weiss, M. Non-equilibrium forces drive the anomalous diffusion of telomeres in the nucleus of mammalian cells. *N. J. Phys.* **19**, 113048 (2017).
74. Benelli, R. & Weiss, M. From sub- to superdiffusion: fractional Brownian motion of membraneless organelles in early C. elegans embryos. *N. J. Phys.* **23**, 063072 (2021).
75. Sunyer, R., Ritort, F., Farré, R. & Navajas, D. Thermal activation and ATP dependence of the cytoskeleton remodelling dynamics. *Phys. Rev. E* **79**, 051920 (2009).
76. Bursac, P. et al. Cytoskeletal remodelling and slow dynamics in the living cell. *Nat. Mater.* **4**, 557 (2005).
77. Allan, D. B., Caswell, T., Keim, N. C., van der Wel, C. M. & Verweij, R. W. Soft-matter/trackpy: Trackpy v0.5.0. *Zenodo* <https://doi.org/10.5281/zenodo.4682814> (2021).

Acknowledgements

R.M. acknowledges the German Science Foundation (DFG, grant no. ME 1535/12-2) for support. M.W. and R.B. acknowledge financial support from VolkswagenStiftung (Az 92738) and the Elite Network of Bavaria (Study Program Biological Physics). C.S. acknowledges the VolkswagenStiftung (Az 96733).

Author contributions

V.S. performed the analytical calculations, the 1D simulations and wrote and reviewed the manuscript. D.K. obtained and analysed the experimental diffusive data and wrote the manuscript. E.M. contributed to the code for 1D simulations. R.S. and F.R. obtained and analysed the experimental superdiffusive data from cytoskeleton fluctuations of living cells. F.T. and C.S.-U. obtained and analysed the experimental superdiffusive data from nanoparticles in hMSCs. R.B. obtained the experimental subdiffusive data. M.W. analysed the subdiffusive data, performed the 2D simulations and wrote the manuscript. R.M. and G.O. designed and supervised the work, and wrote and reviewed the manuscript.

Funding

Open Access funding enabled and organized by Projekt DEAL.

Competing interests

The authors declare no competing interests.

Additional information

Supplementary information The online version contains supplementary material available at <https://doi.org/10.1038/s42005-022-01079-8>.

Correspondence and requests for materials should be addressed to Ralf Metzler.

Peer review information *Communications Physics* thanks the anonymous reviewers for their contribution to the peer review of this work.

Reprints and permission information is available at <http://www.nature.com/reprints>

Publisher's note Springer Nature remains neutral with regard to jurisdictional claims in published maps and institutional affiliations.



Open Access This article is licensed under a Creative Commons Attribution 4.0 International License, which permits use, sharing, adaptation, distribution and reproduction in any medium or format, as long as you give appropriate credit to the original author(s) and the source, provide a link to the Creative Commons license, and indicate if changes were made. The images or other third party material in this article are included in the article's Creative Commons license, unless indicated otherwise in a credit line to the material. If material is not included in the article's Creative Commons license and your intended use is not permitted by statutory regulation or exceeds the permitted use, you will need to obtain permission directly from the copyright holder. To view a copy of this license, visit <http://creativecommons.org/licenses/by/4.0/>.

© The Author(s) 2022